



Velocity and stresses of partially-reflected water waves in the presence of opposing wind

Fabio Addona^{a,*}, Luca Chiapponi^b

^a University of Delaware, School of Marine Science and Policy, Lewes, 19958, DE, USA

^b Università degli Studi di Parma, Parco Area delle Scienze, 181/A, Parma, 43124, Italy

ARTICLE INFO

Keywords:

Partial-reflection
Water waves
Opposing wind
Quadrant analysis
Momentum transfer

ABSTRACT

It is known that long waves (or swell) ruffled by an opposing wind tends to be dissipated, while shorter waves develop on top of them and travel in the wind direction. However, the long waves are mostly considered progressive and the effect of reflection is neglected. We present an experiment study of mechanically generated regular waves in partially-reflective conditions and observed how they interact with wind an opposing. We look at how different reflection conditions and spatial variability affect the water flow and the stresses within it. By breaking down the signal through a triple decomposition, we analyse the velocity components and compare the wave-induced Reynolds stresses with a theoretical model which takes into account partial reflection conditions (Addona et al., 2018). This model helps us understand the spatial variability of the wave-induced stresses and avoid misinterpretations of the experimental results, proving the role the key role of reflection. A quadrant analysis of the fluctuating velocities is performed to study the direction of momentum transfer, which always seems to be from the interface to the water below. The work provides novel experimental data of the flow field of partially-reflected water waves in the presence of wind.

1. Introduction

In ocean, it is common to find swell waves, which travelled far away from their generation area, interacting with winds blowing in whatever direction. Several researchers studied the effect that wind may have on swell, and vice versa (Sullivan and McWilliams, 2010). This is due to the great importance of knowing and predicting sea weather and waves for practical reasons (e.g., for navigation safety or offshore structures design). Studies from field campaign and laboratory experiments, usually focusing on wind in the same or opposing direction, suggest that swell (or monochromatic waves in laboratory) is attenuated by an opposing wind and increased by a following wind, even though wave growth, dissipation rates and their dependencies are not fully understood (Longuet-Higgins and Stewart, 1960; Hasselmann, 1971; Longuet-Higgins, 1987; Belcher et al., 1994; Grare et al., 2013). For instance, in the presence of an opposing wind some experimental measurements and numerical models showed that previous theoretical studies tended to underestimate the attenuation of the regular waves (Peirson et al., 2003; Cao et al., 2020).

However, most of previous studies considered only progressive waves propagating in a single direction. It means that no reflection is taken into consideration. But in many cases, e.g., when swell waves approach the nearshore zone, the shoreline, bottom steps, and other

obstacles may cause reflection of the incoming waves generating a more complex wave field. From an experimental point of view, some previous work showed that considering reflective conditions can affect the free surface statistics and the flow field (Olfateh et al., 2017; Addona et al., 2018). In the simplified case of partially-reflected regular waves, the periodic horizontal and vertical velocities have a phase shift and are not out-of-quadrature anymore, generating a mean shear stress that becomes relevant even with a reflection coefficient as small as 0.1 (in terms of wave height). That stress would be neglected in the absence of an adequate reflection analysis. In the presence of a following wind interacting with a partially-reflected regular wave, it means that the partition of the total stress is changed, since a new term appears (the mean wave shear stress) and partially sustains momentum transfer, potentially either upwards or downwards. The mean wave shear stress is also defined as Reynolds wave(-generated) shear stress, as it involves the periodic (organized) component of the flow. It arises from a triple decomposition technique, which decompose the fluid motion into a mean, a periodic and a turbulent components (Hussain and Reynolds, 1970). Several researchers have tried to estimate this contribution, arriving at varied and contradictory results (Cheung and Street, 1988; Longo and Losada, 2012; Olfateh et al., 2017; Addona et al., 2018). Fig. 1 shows the comparison between the Reynolds wave shear stress

* Corresponding author.

E-mail addresses: faddona@udel.edu (F. Addona), luca.chiapponi@unipr.it (L. Chiapponi).

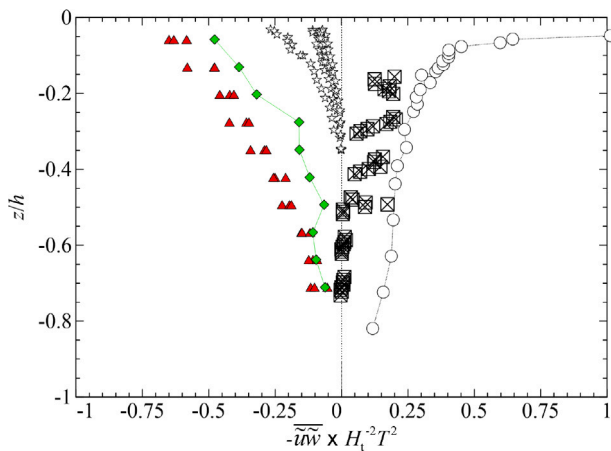


Fig. 1. Vertical profile of the experimental non-dimensional Reynolds wave shear stress: comparison of literature results. \circ Longo and Losada (2012), wind waves; \square Olfateh et al. (2017), mechanically generated waves plus following wind; \star Cheung and Street (1988), mechanically generated waves plus following wind; \diamond Addona et al. (2018), mechanically generated waves without wind; \blacktriangle Addona et al. (2018), mechanically generated waves plus following wind.

of some literature works involving monochromatic and wind waves. We can see that, although the order of magnitude of the scaled stresses is similar, both the intensity and the sign vary. This could be partially explained by the spatial variability (i.e., horizontal inhomogeneity) and velocity phase shift which appear in the presence of reflection, but a close answer has not been reached yet. We remind that in a progressive regular wave, the mean wave shear stress is null.

Guided by the insights of the previous works on swell reflection in the presence of a following wind, Addona et al. (2020) studied the free surface statistics of partially-reflected regular waves interacting with an opposing wind. They have shown that there is a complex dependency between reflection and wind conditions, and that the wave growth related to the fluctuations (i.e., wind) varies with reflective and wind conditions in a non-trivial way, possibly due to non-linear interactions between wind and partially-reflected regular wave. It suggests that a more in-depth analysis of the velocities and stresses would be beneficial. Generally speaking, stresses at the air–water interface are subject to variability due also to different reflective conditions. It theoretically derives from the phase shift of both vertical and horizontal velocities with respect to the free surface elevation (Addona et al., 2018). We expect that reflection conditions, which modifies the magnitude and the sign of the wave stresses, influence the dynamic boundary conditions, which links the stresses at the interface. In turn, this would have an impact on the momentum and energy transfers between air and water.

In this work, we make a step forward and experimentally study how velocity and stresses are influenced by an opposing wind. Several tests with monochromatic mechanically generated waves were performed controlling the reflection coefficient. For one of the reflective conditions, also the spatial variability was considered by repeating the measurements in different cross-sections. We remark that in Addona et al. (2018) it has been shown that changing the section of the velocity measurements would change the pattern of the wave mean stress profile, in a similar way to changing reflection conditions.

Fig. 2 reports a road map of the activities for a better comprehension. We focus our study on the velocity field and the stresses components, highlighting two main aspects: the effects of different reflection coefficients, and the spatial variability of the stresses. We adopt a triple decomposition technique to discriminate the contribution of the mean (current), periodic (wave) and turbulent (wind) components. Thus, we analyse velocity and stresses that stem from the triple decomposition of the wave field.

The paper is structured as follows. In Section 2 we describe the experimental set-up, the instruments used and the activity, while in Section 3 we report details on the data analysis techniques. Section 4 shows the results of the experiments measurements and data analysis, along with some discussion of what has been observed. Finally, Section 5 reports the conclusions of the present work.

2. Experiments

Two sets of experiments were performed in the Ocean–Atmosphere Interaction Flume (Canal de Interacción Atmósfera-Océano, CIAO), at the Instituto Interuniversitario de Investigación del Sistema Tierra en Andalucía (IISTA), Granada (ES). The facility consists of (i) a wave flume with two piston-type paddles for the generation and the active absorption of water waves, (ii) a closed-loop wind tunnel which generates air at different speeds above the free water surface, (iii) a current generator and (iv) a rain generator. Notice that the current and rain generators were kept off during the present activity.

A two-dimensional Laser Doppler Anemometer (LDA) was used to measure the horizontal and vertical components of the water velocity at ten equally-spaced points along a vertical, with a data acquisition duration of 330 s for each run (i.e., for each measure). Observations focused on the water side, at depths larger than the amplitude of the mechanically generated wave. Eight ultrasonic (US) probes were also used to measure the water surface displacement, and they were placed at a distance from each other which allows the signals to be correlated. In fact, we calculated the reflection parameters thanks to three US gauges, following the method of Mansard and Funke (1980) as modified by Baquerizo (1995). A sketch of the experimental apparatus is illustrated in Fig. 3. The reference system is defined by the horizontal coordinate x , positive in the wind direction, and the vertical coordinate z , equal to zero at the still water level (SWL) and positive upwards. The air friction velocity, u_{*e} , was calculated as a fitting parameter of the logarithmic wind speed profile, with the velocity measurements obtained by means of a Pitot tube (not shown here). More details can be found in Addona et al. (2018, 2020).

The experiments consisted of mechanically generated waves under different reflection conditions and in the presence of an opposing wind. The nominal height and period of the incident wave, as well as wind speed, were nominally the same for all the tests. In the first set of experiments (Expt. MGoW1–2a–3–4–5, where MGoW stands for “Mechanically-Generated opposing Wind waves”), the LDA system was located in a fixed x/L position, where L is the wave length computed from the linear dispersion relation, while the reflection parameters (K_r and $\Delta\phi$) were changed by means of the active absorption system. The second set (MGoW2a–d) was characterized by the same wave conditions of Expt. MGoW2a, but the LDA was moved in different positions along the non-dimensional x/L coordinate, to evaluate the spatial variability of the Reynolds wave stresses. The experimental parameters are reported in Table 1.

3. Data processing

3.1. Pre-processing and triple decomposition

A pre-processing of the signal is needed to overcome two possible source of errors: non-fixed data rate and outliers. The former is solved by interpolating the raw signal on a fixed time stamp, with a sampling time equal to the inverse of the mean data rate (defined, for each run, as the ratio of the total number of samples to the data acquisition duration). Then, a despiking algorithm, developed by Goring and Nikora (2002) and modified by Mori et al. (2007), is used to identify and remove outliers from LDA data series.

Each velocity signal is split into three parts (see Hussain and Reynolds, 1970):

$$v(x, z, t) = \bar{v}(x, z) + \tilde{v}(x, z, \tau) + v'(x, z, t) \quad (1)$$

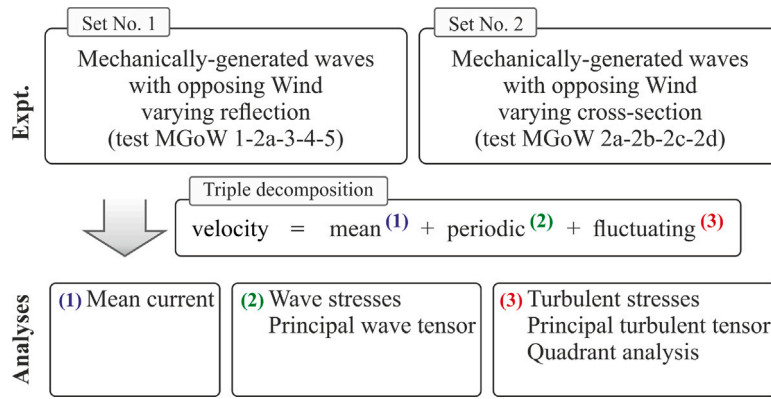


Fig. 2. Road map of the present paper activities.

Table 1

Parameters of the experiments. MGoW stands for “Mechanically-Generated opposing Wind waves”; u_w is the friction velocity, H_t is the total wave height, H_i is the incident wave height, T is the period of the paddle oscillation, K_r , and $\Delta\varphi$ are the reflection coefficient and the phase shift, respectively. The relative coordinate x/L indicates the LDA measurement section (position) with respect to US2 (see Fig. 3).

Expt.	u_w (cm s ⁻¹)	x/L	H_t (cm)	H_i (cm)	T (s)	$K_{r,w}$	$\Delta\varphi$ (rad)
MGoW 1	75	0	6.3 ± 0.1	4.8 ± 0.1	1.6	0.843 ± 0.010	0.86 ± 0.10
2a	75	0	6.3 ± 0.1	5.3 ± 0.1	1.6	0.658 ± 0.005	0.90 ± 0.03
2b	75	0.04	7.7	5.2	1.6	0.671	0.86
2c	75	0.09	8.5	5.2	1.6	0.673	0.86
2d	75	0.13	8.6	5.1	1.6	0.671	0.85
3	75	0	5.7	5.8	1.6	0.337	1.06
4	75	0	5.1	5.5	1.6	0.132	1.53
5	75	0	4.9	5.4	1.6	0.099	2.95

representing respectively the mean (current), the periodic (wave) and the fluctuating (turbulence) component. The mean component is extracted by time averaging the velocity signal as follows:

$$\bar{v}(x, z) = \frac{1}{T_D} \int_0^{T_D} v(x, z, t) dt, \quad (2)$$

where T_D is the data acquisition duration. The periodic component is obtained by phase averaging the velocity measurements at the net of the mean flow:

$$\bar{v}(x, z, \tau) = \langle v - \bar{v} \rangle = \frac{1}{N_w} \sum_{n=1}^{N_w} (v(x, z, \tau + nT) - \bar{v}(x, z)), \quad (3)$$

where τ is the wave phase, T is the regular wave period and N_w is the number of waves recorded during one test. Then, the fluctuating component is taken as the remaining part of the velocity signal after subtracting the time and phase averages:

$$v'(x, z, t) = v(x, z, t) - \bar{v}(x, z) - \bar{v}(x, z, \tau). \quad (4)$$

3.2. Velocity covariance

We are interested in evaluating the velocity components products, which are related to the stresses through the dynamic viscosity ρ of the fluid. The time average of the experimental velocity correlations (covariances), for periodic, mixed and fluctuating components, reads:

$$\overline{\bar{v}_i \bar{v}_j}(x, z) = \frac{1}{T} \int_0^T \bar{v}_i \bar{v}_j dt, \quad (5)$$

$$\overline{\bar{v}_i v'_j}(x, z) = \frac{1}{T} \int_0^T \bar{v}_i v'_j dt, \quad (6)$$

$$\overline{v'_i v'_j}(x, z) = \frac{1}{T_D} \int_0^{T_D} v'_i v'_j dt, \quad (7)$$

where i, j can be either 1 or 2 for, respectively, horizontal and vertical velocities (i.e., $v_1 = u$ and $v_2 = w$). By definition, the mixed correlations

are null, i.e., $\overline{\bar{v}_i v'_j} = 0$ (Hussain and Reynolds, 1970). The wave-induced (tilde) and fluctuating (prime) components form the wave and turbulent Reynolds stress tensor, respectively. Equal indices i, j result in diagonal components of the tensors, while different indices represent shear stress.

3.3. Quadrant analysis

Quadrant analysis is a useful technique to get more information about momentum exchange between the turbulent boundary layer and the outer flow (see, e.g., Wallace, 2016). This technique consists of a characterization of the turbulent field by considering the permanence of the fluctuating velocities u' and w' in the four quadrants, defined by the sign of the fluctuating components. Here, we consider the inner domain of the water, and we adopt the following convention: (i) an ejection is defined as outward movement of low-speed fluid; (ii) sweep is high-speed fluid moving towards the boundary, accordingly to Longo et al. (2012a). In particular, for our reference system, we have ejections when $u' < 0, w' < 0$ and sweeps when $u' > 0, w' > 0$ (see Fig. 4). The other two possible conditions, $u' < 0, w' > 0$ and $u' > 0, w' < 0$, are defined as inward and outward interactions, respectively.

We calculate the contribution given by each quadrant to the total shear stress as

$$S_j = \frac{1}{N_j} \sum_{i=1}^{N_j} [u'_i w'_i]_j, \quad j = 1, \dots, 4, \quad (8)$$

where N_j is the number of samples belonging to the j th quadrant. The average stress of the j th quadrant is

$$\overline{u' w'}_j = \frac{1}{N} \sum_{i=1}^{N_j} [u' w']_j, \quad j = 1, \dots, 4 \quad (9)$$

where N is the total number of samples and the index i is omitted. Eq. (9) can also be written as

$$\overline{u' w'}_j = \frac{N_j}{N} S_j, \quad j = 1, \dots, 4 \quad (10)$$

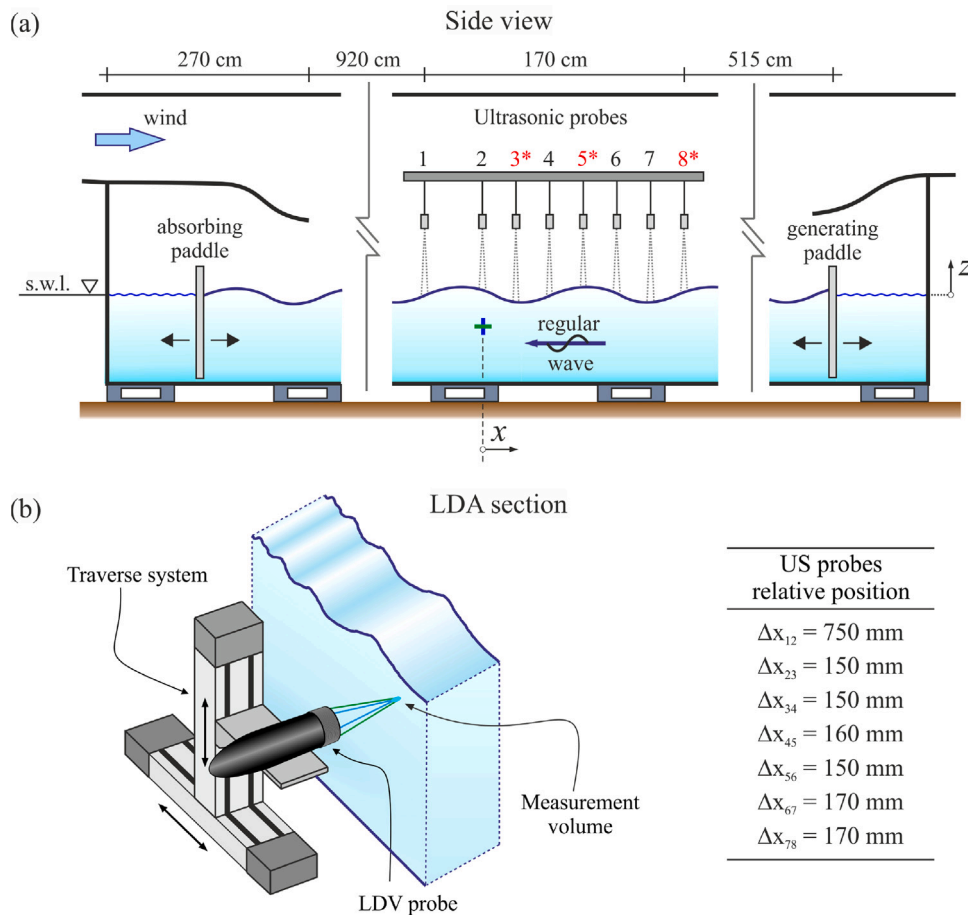


Fig. 3. Sketch of the experimental apparatus: a side view of the flume (a) and a prospective view of the Laser Doppler velocimetry (LDA) system (b). Probes US3-5-8 were used for the reflection analysis. x and z determine the reference system, positive in the wind direction and pointing upwards starting from the still water level (s.w.l.), respectively.

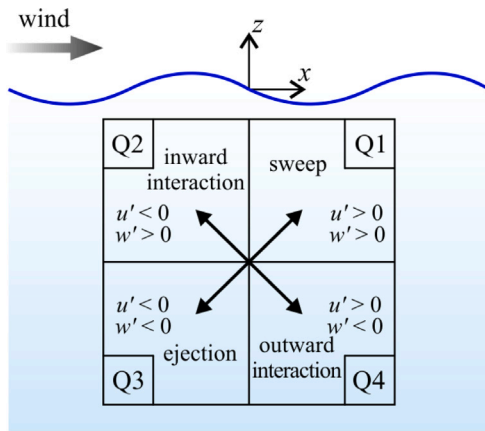


Fig. 4. Quadrant decomposition of the fluctuating components of velocity.

where the ratio N_j/N is the relative permanence of the event in the j th quadrant, and the total shear stress results

$$\overline{u'w'} = \sum_{j=1}^4 \overline{u'w'_j} \quad (11)$$

The introduction of a threshold for the analysis of the results can be helpful in the description of bursting, which consists of highly-intermittent and also explosive events carrying most of the momentum from the boundary layer to the mean flow (and vice versa). We consider

the events that satisfy the following relation:

$$u'w' > M u'_{rms} w'_{rms} \quad (12)$$

where the parameter M determines the threshold. Considering a fixed threshold, the concentration of the j th quadrant is

$$C_j^M = \frac{1}{N} \sum_{i=1}^N \phi_{j,i}^M \quad (13)$$

with the coefficient $\phi_{j,i}^M$ defined as

$$\phi_{j,i}^M = \begin{cases} 1 & \text{if } u'w' > M u'_{rms} w'_{rms} \text{ and belongs to the } j\text{th quadrant} \\ 0 & \text{otherwise} \end{cases} \quad (14)$$

Thus, we can define the phasic-averaged Reynolds shear stress for the j th quadrant as

$$\widehat{u'w'_j}^M = \frac{\sum_{i=1}^N (u'w')_i \phi_{j,i}^M}{\sum_{i=1}^N \phi_{j,i}^M} \quad (15)$$

and the time-averaged Reynolds shear stress as

$$\overline{u'w'_j}^M = \frac{1}{N} \sum_{i=1}^N (u'w')_i \phi_{j,i}^M = C_j^M \left(\widehat{u'w'_j}^M \right)^M \quad (16)$$

Note that here the phasic-averaged term is conditioned by the threshold M , and not by the phase of the flow (air or water, see Longo et al., 2012a). Eq. (16) can be expressed as stress fraction

$$F_j^M = \left(\overline{u'w'_j}^M \right)^M / \overline{u'w'} \quad (17)$$

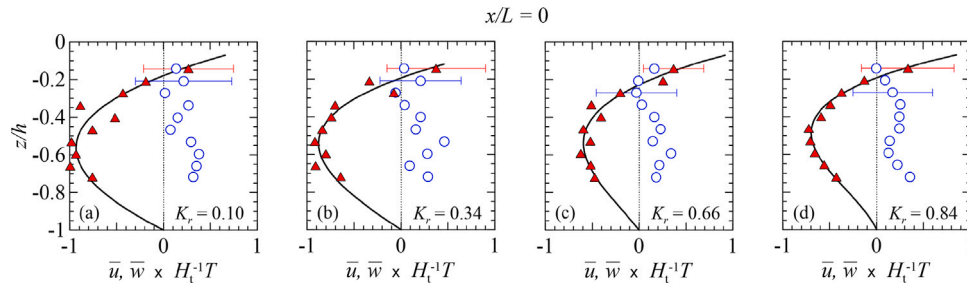


Fig. 5. Non dimensional mean velocity for experiments MGoW1-2a-3-5 (different reflective conditions, same LDA section). Filled triangles and empty circles represent the velocity components along the horizontal and vertical direction, respectively. Solid curves are a third-order polynomial fitting of the horizontal velocity with no-slip condition at the bottom, while error bars refer to one standard deviation.

which yields

$$\sum_{j=1}^4 F_j^0 = 1. \tag{18}$$

4. Results and discussion

4.1. Influence of reflection on mechanically-generated opposing wind waves

The mean velocities and the stresses are shown below and commented separately for each experimental condition, while the free surface statistics referring to the same tests were already analysed in Addona et al. (2020) and not reported here. The description of the flow field under varying reflection conditions will be given first.

4.1.1. Mean velocity

Nonzero mean velocities indicate the presence of currents that develop inside the wave flume. The main interest is generally focused on the horizontal current, which is strongly influenced by the atmospheric forcing, as wind blowing from the left to the right is expected to set up a forward and a return drift current. We bear in mind that the mean horizontal and vertical velocities also arise from other sources, as (i) the non-linear effects of the regular wave between troughs and crests, (ii) the finite length of the wave flume, (iii) the secondary circulations which take place in the presence of wind and partial reflection.

In all present experiments, the typical profile for a wind-induced current is observed: the horizontal mean velocity, \bar{u} , is positive near the surface (i.e., it is in the same direction as the airflow, as a direct consequence of drag), while it becomes negative as depth increases in order to fulfil the mass conservation for a finite-length domain (see Fig. 5). On the other hand, the vertical mean velocity, \bar{w} , is slightly negative in proximity of the air–water interface, while it is always positive toward the bottom. The same behaviour was observed for experiments in the case of following wind (Addona et al., 2018). In the case of a closed tank with the tangential stress acting on the free surface, a vertical positive velocity component is expected at small fetches, and a vertical negative velocity component is expected at larger fetches (Longo et al., 2012b). However, longitudinal and transversal circulation (e.g., Langmuir cells), due to the action of wind and once again to the finite length of the channel, can influence the mean flow field resulting in a deviation from such a scheme. Such a complex scenario precludes drawing conclusions about the net momentum transfer due to the average velocity components.

As regards the influence of reflection, we observe that the non-dimensional horizontal mean velocity decreases as the reflection coefficient increases.

4.1.2. Wave-induced stresses

The wave-induced stresses are the components of the wave-induced stress tensor, which takes into account only the periodic component of the velocity, \tilde{u} and \tilde{w} . By applying the time and the phase average to the momentum equations, it is possible to separate the contribution of the wave-induced stress tensor, with normal components $\overline{\tilde{u}\tilde{u}}$, $\overline{\tilde{w}\tilde{w}}$ and shear components $\overline{\tilde{u}\tilde{w}}$, to the contribution of the turbulent stress tensor (which will be discussed in the next section). From the theoretical model of Addona et al. (2018) at the first order, the vertical profile of the wave shear stress can be expressed as

$$\overline{\tilde{u}\tilde{w}} = gka_i^2 \frac{\sinh [2k(z+h)]}{\sinh (2kh)} K_r \sin(2kx + \Delta\varphi), \tag{19}$$

where g is the gravitational acceleration, k is the wave number obtained from the relation dispersion, a_i is the incident wave amplitude and h is the water depth. We highlight that the term $\overline{\tilde{u}\tilde{w}}$ is null for progressive waves, while it appears in the presence of partial reflection. It has been shown in previous works that neglecting this term can lead to significant errors in the interpretation of experimental data, even for small values of the reflection coefficient and phase shift (Olfateh et al., 2017; Addona et al., 2018).

Fig. 6(a–d) shows the comparison between theoretical and experimental values of $\overline{\tilde{u}\tilde{w}}$. The results show that the wave shear stress is responsible for momentum transfer with different sign and intensity depending on the reflection conditions, and its value can be predicted thanks to the theoretical analysis.

In our activity, we obtained two different free-surface acquisitions for each experiment: one with mechanically generated waves only (before starting the wind) and one with mechanically generated waves plus opposing wind. Therefore, two different vertical profiles of the theoretical $\overline{\tilde{u}\tilde{w}}$ can be calculated. Fig. 6(a–d) also shows the comparison between theoretical results calculated in the presence/absence of the wind. A non-negligible difference is observed between the two cases, with significant changes in the vertical profile of wind-induced stresses. This result confirms that the presence of opposing wind modify the reflection coefficient K_r and the phase shift $\Delta\varphi$, as reported in Addona et al. (2020). Furthermore, it also affect the wave shear stress and, consequently, the net momentum transfer and the stress partitioning in the proximity of the interface between air and water.

The terms $\overline{\tilde{u}\tilde{u}}$ and $\overline{\tilde{w}\tilde{w}}$ represent the diagonal components of the wave-induced stress tensor. The horizontal wave normal stress reads

$$\overline{\tilde{u}\tilde{u}} = gka_i^2 \frac{\cosh [k(z+h)]}{\sinh (2kh)} [1 + K_r^2 - 2K_r \cos(2kx + \Delta\varphi)], \tag{20}$$

while the vertical wave normal stress is

$$\overline{\tilde{w}\tilde{w}} = gka_i^2 \frac{\sinh [k(z+h)]}{\sinh (2kh)} [1 + K_r^2 + 2K_r \cos(2kx + \Delta\varphi)]. \tag{21}$$

Fig. 6(e–h) shows the vertical profile of the wave normal stresses, both of which show fair agreement with the theoretical model. We also notice that the horizontal normal stress $\overline{\tilde{u}\tilde{u}}$ is more affected by different reflective conditions, while the vertical component $\overline{\tilde{w}\tilde{w}}$ is almost constant for all experiments.

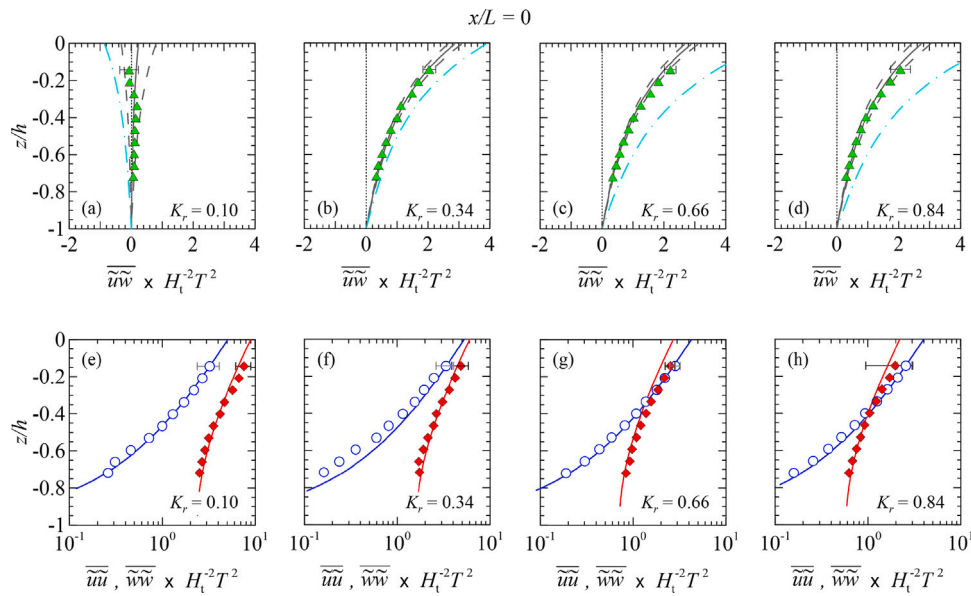


Fig. 6. Vertical profiles of the wave-induced shear stresses (panels a–d) and of the wave-induced normal stresses (panels e–h) for experiments MGoW1–2a–3–5 (different reflective conditions, same LDA section). Solid lines represent the theoretical values, dashed lines the 95% confidence interval and dashed-dotted lines the theoretical values for experiments in identical conditions except for the absence of wind. Symbols are experimental data: for panels e–h, red filled diamonds and blue empty circles are horizontal and vertical components, respectively.

4.1.3. Turbulent stresses

The fluctuating velocities u' and w' are obtained after subtracting the phase and time averages from the LDA signal, so that we can evaluate the turbulent stress tensor, with normal components $\overline{u'u'}$, $\overline{w'w'}$ and shear component $\overline{u'w'}$.

Fig. 7(a–d) shows the turbulent shear stress distribution along a vertical profile. It can be seen that an opposing wind is responsible for negative turbulent shear stresses near the surface, suggesting a net momentum transfer downwards (from air to water). The mean turbulent shear stress $\overline{u'w'}$ goes to zero at $\approx 0.35 z/h$ in the case of $K_r = 0.84$. As reflection decreases, the turbulent shear stresses increase and reach shallower depths, going to zero at around half the water column for $K_r = 0.13$. Since the wind action is the main forcing of the fluctuating stress at the surface, it is not surprising that also for mechanically generated waves with opposing wind the turbulent shear stress yields a momentum transfer from the wind to the wave.

Fig. 7(e–h) shows that the normal turbulent stresses increase approaching the free surface, since much of the turbulent kinetic energy is concentrated at the air–water interface. As the depth increases, the normal stresses decrease toward a constant value, indicating a rotation of the turbulent stress tensor. It is possible to observe that (i) the horizontal normal stress, $\overline{u'u'}$, is slightly larger than the vertical one, $\overline{w'w'}$, so that the dominant component is aligned with the wind direction, and (ii) higher reflection coefficients are associated with lower values and a lower variability (i.e., smaller deviations) of the normal stresses. In the absence of wind, it was previously found that the maximum is reached at $z/h \approx 0.3$, possibly due to recirculating cells developing in the finite-length laboratory facility (not reported here).

In general, the study of the turbulent stress tensor components indicates that reflection acts as a constraint on the turbulent flow field induced by an opposing wind. This means that, under conditions of weak reflection the turbulent stresses are larger, with higher deviations and they diffuse deeper; vice versa, in the case of stronger reflection the turbulent stresses present lower values and less variability.

4.1.4. Quadrant analysis

The momentum transfer direction and intensity were further investigated through a quadrant analysis. The quadrant analysis is helpful to quantify the contributions of the Reynolds turbulent shear stress to the

turbulent momentum exchange by considering the signs of u' and w' . We called “sweeps” and “ejections” the events attributed to the first quadrant (u' and w' both positive) and the third quadrant (u' and w' both negative), respectively. Events related to the second ($u' < 0$ and $w' > 0$) and fourth ($u' > 0$ and $w' < 0$) quadrants were called outward and inward interaction, respectively.

Fig. 8 shows the vertical profiles of the quadrant-averaged shear stress. The contributions from each quadrant are of the same order of magnitude, even if quadrants Q2 and Q4 have slightly higher values than quadrants Q1 and Q3, indicating that momentum is transferred downwards from the interface (especially in the case of a low reflection coefficient). The difference between the various quadrants will appear more evident below, when the data will be processed according to the threshold described in Section 3.3. The same result was observed in the turbulent structure of the water side by Longo et al. (2012a), whereas several studies of the airflow above water waves reported ejections and sweeps as the main contributors to the transfer of momentum and turbulent kinetic energy in the turbulent boundary layer (Kline et al., 1967; Wallace and Brodkey, 1977; Li and Bou-Zeid, 2011).

Regardless of the quadrant, we also observe that (i) the value of the contributions increases for decreasing reflection coefficient, and (ii) stronger events took place near the free surface (i.e., where wind is more effective). Away from the interface, the quadrant-averaged stresses are characterized by a lower intensity, they are quite uniform along the vertical, and each quadrant gives an equal contribution to the total shear stress (which consequently becomes zero).

The average shear stress was also calculated as a function of the parameter M , which determines the threshold above which bursting events are considered. Fig. 9 shows the results for experiments MGoW1 and MGoW4. Again, the main contribution to the total shear stress is from quadrants Q2 and Q4, with a major momentum transfer from the air to the water side. The higher values of the average shear stress typically take place in proximity of the free surface. However, for experiment MGoW4, we notice that the turbulent shear stresses are relevant also far from the interface (at $z/h \approx -0.3$), suggesting that the turbulent momentum injection could impact deeper water levels.

4.1.5. Principal axes of the Reynolds stress tensors

The wave and the turbulent stress tensors are both of the second-order and symmetric, so it is possible to represent them as matrices

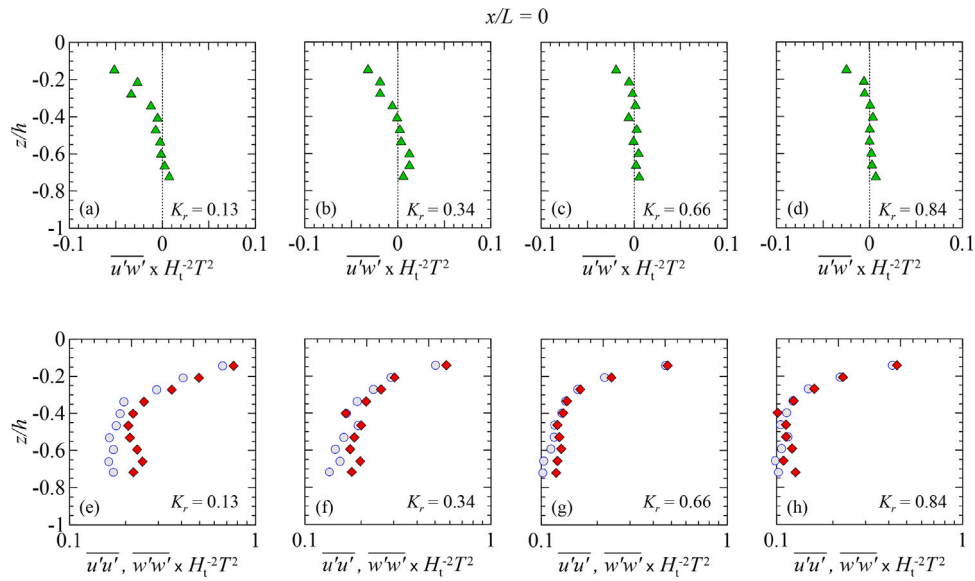


Fig. 7. Vertical profiles of the turbulent shear stress (panels a–d) and of the turbulent normal stress (panels e–h) for experiments MGoW1–2a–3–4 (different reflective conditions, same LDA section). Symbols are experimental data: red filled diamonds and blue empty circles are horizontal and vertical components, respectively. Error bars refer to one standard deviations.

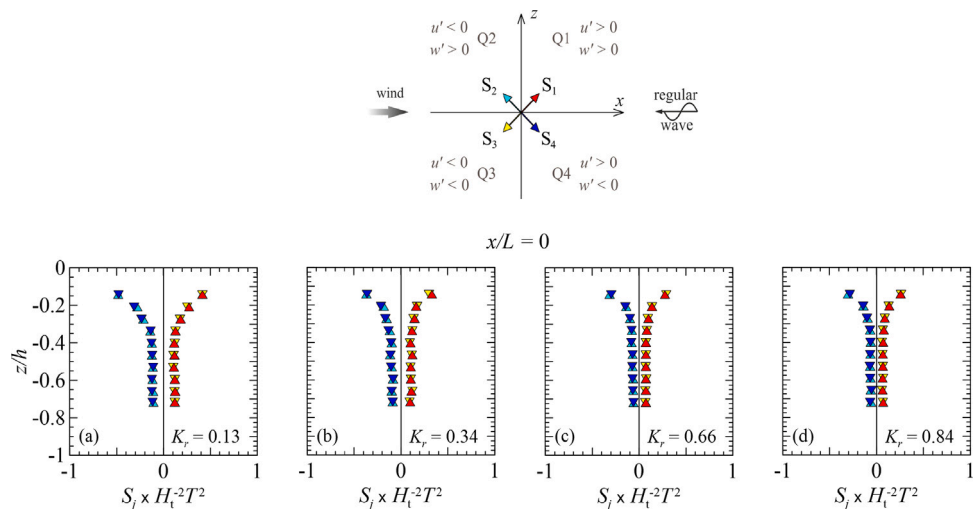


Fig. 8. Quadrant-averaged shear stresses for experiments MGoW1–2a–3–4 (different reflective conditions, same LDA section). Each panel refers to a different reflection condition.

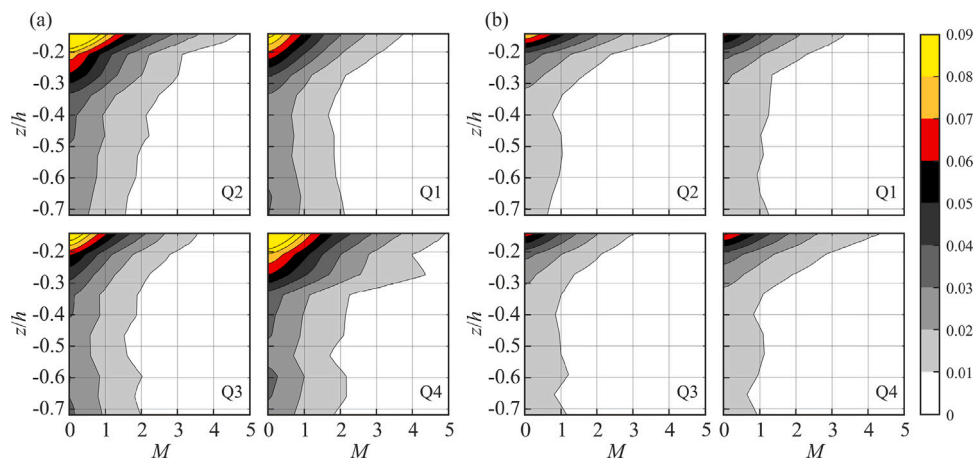


Fig. 9. Time-averaged Reynolds shear stress in each quadrant decomposed with increasing threshold M . Panels (a) and (b) refers to Experiments MGoW4 and MGoW1, respectively.

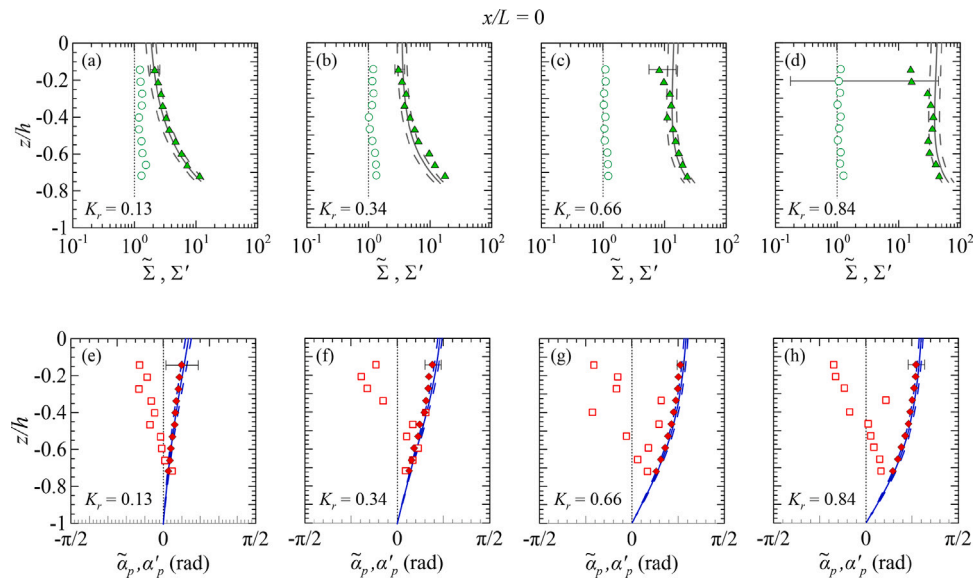


Fig. 10. Experiments MGoW1-2a-3-4 (different reflection, same LDA section). Panels (a-d) show the ratio of the maximum to minimum principal stress, $\tilde{\Sigma}$ and Σ' . Symbols are experimental data: the wave (turbulent) component is represented by filled green triangles (green empty circles). Panels (e-h) show the orientation of the principal stresses, $\tilde{\alpha}_p$ and α'_p . The wave (turbulent) component is represented by filled red diamonds (red empty squares). Error bars refer to one standard deviation. Solid lines are theoretical values and dashed lines are 95% confidence intervals.

and diagonalize them. In that way, we obtain the principal stresses σ_{max} and σ_{min} and the principal angle α_p (i.e., the diagonal terms and the orientation of the principal stresses with respect to the Cartesian coordinates $x-z$, respectively). We notice that the actual flow field is three-dimensional, hence in our experiments we had a reduced perspective of its structure since we limited the analyses on the streamwise and vertical velocities, u and w , assuming negligible the effects of the spanwise component, y . For the wave stress tensor, the analytical model yields a theoretical representation of the principal stresses and principal angle, and theoretical profiles could be compared to the experimental values. For the turbulent stress tensor, only the experimental values are available.

Fig. 10(a-d) shows the ratio of the maximum to the minimum principal stress, $\Sigma = \sigma_{max}/\sigma_{min}$, which offers a synthetic view of the isotropy of the second-order stress tensors. The wave principal stresses are well approximated by theory, and the trend along the vertical is similar for different reflective conditions, but it is evident that a stronger reflection causes a shift towards larger values of the ratio $\tilde{\Sigma}$ (i.e., the anisotropy increases with reflection coefficient). The turbulent principal stresses ratio, Σ'_{min} , is close to unity for all the Experiments, suggesting a pronounced isotropy along the entire vertical profile.

Fig. 10(e-h) shows the orientation of the principal wave (and turbulent) stresses. In the case of the wave component, the vertical profile is modulated by the different reflective conditions and results are consistent with the theoretical model. It can also be observed that the principal angle, $\tilde{\alpha}_p$, increases for increasing reflection coefficient. With reference to the principal turbulent stresses, the experimental evidence shows that α'_p is approximately zero for $z/h < 0.5$ and then increases upward, tending to $\pi/4$ near the free surface. These results suggest that an uniform shear rate current is dominant near the free surface for opposing wind; a similar trend has also been observed in mechanically generated waves with following wind (not shown here).

4.2. Spatial variability of mechanically generated opposing wind waves

Here, we first report a comparison between theoretical and experimental wave-induced stresses. Then, we show the spatial variability of the turbulent stresses (including the quadrant analysis) and of the principal stress tensor.

4.2.1. Wave-induced stresses

As shown in Addona et al. (2018), the reflection-induced spatial modulation of the wave stresses could resemble the effects of different reflective conditions in the wave field. This is a relevant factor in the experimental activity, since it should always keep in mind that, under some circumstances (e.g., undesired partial reflection), one single measurement section could be not representative of the entire flow field. We analysed the spatial variability of velocity covariance by varying the LDA measurement section along the flume, keeping constant the reflective conditions.

Fig. 11(a-d) shows the vertical profiles of $\overline{u\tilde{u}}$ along the channel, and it is possible to observe a significant change in the intensity and direction of the results, even if the reflection coefficient is the same. Thus, the estimate of the air-sea momentum transfer may be misinterpreted due to the position of the measurements section. The results show also that reflection induces a spatial variation of the normal stresses along x (panels e-h of Fig. 11) and affects more $\overline{u\tilde{u}}$ than $\overline{w\tilde{w}}$.

Fig. 12(a-d) shows the spatial variation of the principal stresses ratio $\tilde{\Sigma}$ (periodic component), while Fig. 12(e-h) shows the principal angles $\tilde{\alpha}_p$. Once again, the analysis of the experimental results proves that the spatial variability is relevant both close to the free surface and towards the bottom. This further confirms that the spatial modulation in the presence of partial reflection, i.e. in most of real coastal engineering problems, should not be ignored for a correct evaluation of the wave stresses.

4.2.2. Turbulent stresses

Fig. 13(a-d) shows the vertical profile of turbulent shear stress $\overline{u'w'}$, while Fig. 13(e-h) shows the turbulent normal horizontal $\overline{u'u'}$ and vertical $\overline{w'w'}$ stresses. The shear stress exhibits negative values with intensity that increases towards the surface, which indicates downward momentum transfer, while $\overline{u'u'}$ is approximately null from $z/h \approx 0.4 - 0.5$ to the lower bound of the observed domain. Also the normal stress profiles shows higher intensity near the surface, while they tend to a constant value towards the bottom. In both cases, we notice that the magnitude of the stresses changes as a function of the LDA measurements section. This is due to the spatial variability of the total wave height H_t , that is the chosen length scale; since H_t varies with the measurements section, the relative intensity of the turbulent stresses

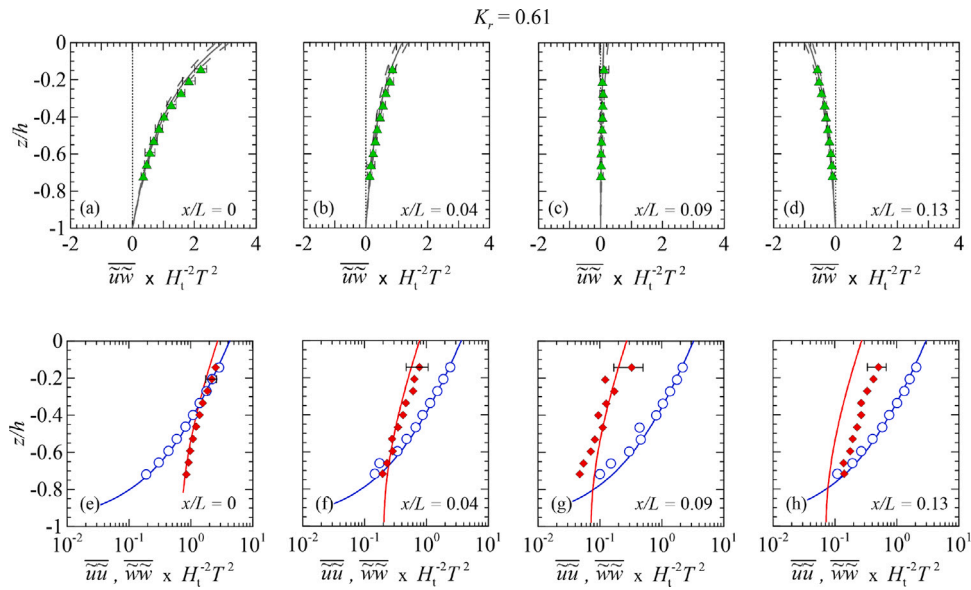


Fig. 11. Vertical profile of the wave velocity covariance \overline{uw} (panels a–d) and vertical profile of the wave normal stresses (panels e–h) for Experiments MGoW2a–d (same reflective condition, different LDA section). Symbols are experimental data: red filled diamonds and blue empty circles are horizontal \overline{uu} and vertical \overline{ww} normal components, respectively. Error bars refer to one standard deviation. Solid lines represent theoretical values, while dashed lines are the 95% confidence interval.

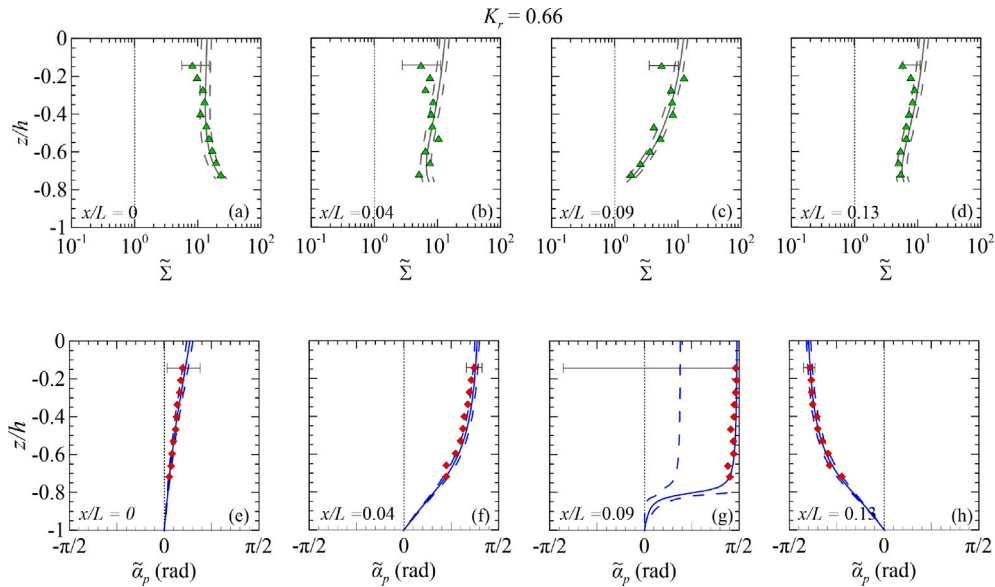


Fig. 12. Experiments MGoW2a–d (same reflective conditions, different LDA section). Panels (a–d) show the ratio of the maximum to minimum principal stress, $\tilde{\Sigma}$. Symbols are experimental data. Panels (e–h) show the orientation of the principal stresses, $\tilde{\alpha}_p$. Error bars refer to one standard deviation. Solid lines are theoretical values and dashed lines are 95% confidence intervals.

changes inversely. This means that, even in the case of equal dimensional values, for a higher total wave height the relative contribution of the turbulent stresses is smaller.

5. Conclusions

We report experiments of mechanically generated waves forced by wind under partially-reflective conditions.

The evaluation of the mean currents does not give us many insights about the effects of reflection. However, we can notice that a typical wind-induced shear current develops throughout the water column, with positive values (compared to the wind direction) close to the

surface, and negative values towards the bottom. A similar information is suggested by the turbulent principal angles, i.e., that the shear rate current is dominant at the surface and determines a rotation of the principal axes. Further details on the turbulent flow of the wind waves are also extrapolated through the quadrant analysis. The outward-inward interactions are slightly prevalent in the physical process, and a net transfer of momentum from air to water is observed in the presence of an opposing wind. This fact would be probably more evident near the free surface, i.e., between trough and crest, where, however, we lack measurements.

The most interesting results stem from the wave-induced and turbulent stresses. The results clearly indicate that wave stresses mainly

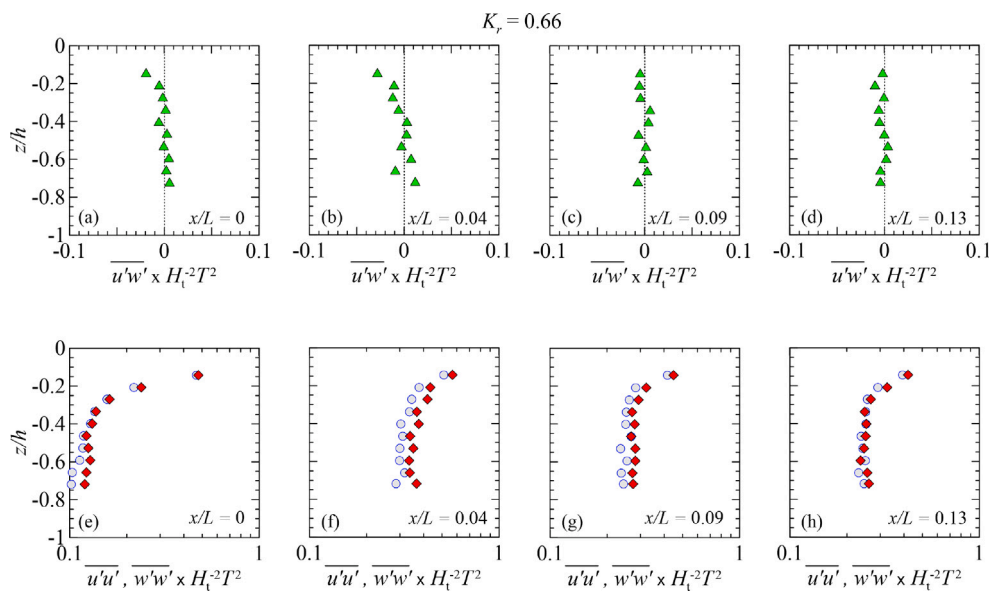


Fig. 13. Vertical profile of the turbulent shear stress (panels a–d), and of the turbulent normal stress (panels e–h) for Experiments MGoW2a–d (same reflective conditions, different LDA section). Symbols are experimental data: red filled diamonds and blue circles are the horizontal $\overline{u'u'}$ and vertical $\overline{w'w'}$ component, respectively. Error bars refer to one standard deviations.

depend on two factors: (i) the different reflection conditions and (ii) the specific measurement section (i.e., a spatial variability is present and it must be considered for the interpretation of the results). Both aspects are predicted by the theoretical model, and the agreement between theory and experiments is fairly good. In particular, reflection controls the spatial variability and creates a sequence of alternating sign vertical profiles for $-\overline{u'w'}$. The horizontal spatial average of Reynolds wave shear stress is expected to give null contribution only if it is extended for several wave lengths, and only in the case of horizontal homogeneity. In case of reflection, those hypotheses are not true anymore, hence reflective conditions and spatial variability become important.

We highlight that the velocities are non-dimensional with respect to H_i/T . That scaling allows us to link the turbulent component to a velocity scale depending on the reflective conditions. In particular, the square of the velocity scale can be interpreted as the kinetic energy of the wave component, thus the non dimensional turbulent normal stresses represent the rate of the turbulent kinetic energy with respect to the wave component. These rates decrease for increasing reflection, indicating that turbulent kinetic energy is less relevant for higher reflective conditions. In addition, the absolute values of the turbulent stresses also increase for decreasing reflection, which means that turbulent momentum transfer under opposing wind action is more effective for lower reflective conditions. All these results suggest that reflection acts as a constraint to the turbulence. Although in the present experiments it was not possible to measure velocity at a close boundary between air and water, we expect that the dynamic boundary condition at the water surface would be strongly influenced by the phase shift induced by reflective conditions. Accordingly, we expect a different partition of the stresses, momentum and energy transfer in the presence of partially-reflected waves.

This analysis reports that, although all the involved quantities show a complex dependence on wind, reflection and spatial variation, partially-reflected waves exhibit features that can be accurately predicted also in the presence of an opposing wind. Novel aspects of the momentum transfer between wind, wave and water are described, even though the main limits of the experiments were to obtain measurements close to the water surface, i.e., between the crest and the trough. Thus, further studies specifically designed to investigate air-sea interaction would help clarify the effects of different wind speed and direction on partially-reflected water waves.

CRedit authorship contribution statement

Fabio Addona: Conceptualization, Methodology, Software, Validation, Formal analysis, Investigation, Data curation, Writing – original draft, Writing – review & editing, Visualization. **Luca Chiapponi:** Software, Validation, Writing – review & editing, Supervision.

Declaration of competing interest

The authors declare that they have no known competing financial interests or personal relationships that could have appeared to influence the work reported in this paper.

Data availability

Data will be made available on request.

Acknowledgements

The authors would like to thank Maria, Sandro and Miguel for their help and useful discussions, which have given a precious contribution to the realization of the present manuscript.

References

- Addona, F., Chiapponi, L., Clavero, M., Losada, M.A., Longo, S., 2020. On the interaction between partially-reflected waves and an opposing wind. *Coast. Eng.* 162, 103774.
- Addona, F., Lira-Loarca, A., Chiapponi, L., Losada, M.A., Longo, S., 2018. The Reynolds wave shear stress in partially reflected waves. *Coast. Eng.* 138, 220–226.
- Baquerizo, A., 1995. Reflexión del Oleaje en Playas. Métodos de Evaluación y de Predicción (Ph.D. thesis). Universidad de Cantabria, Santander.
- Belcher, S.E., Harris, J.A., Street, R.L., 1994. Linear dynamics of wind waves in coupled turbulent air–water flow. Part 1. Theory. *J. Fluid Mech.* 271, 119–151.
- Cao, T., Deng, B.-Q., Shen, L., 2020. A simulation-based mechanistic study of turbulent wind blowing over opposing water waves. *J. Fluid Mech.* 901.
- Cheung, T., Street, R., 1988. The turbulent layer in the water at an air–water interface. *J. Fluid Mech.* 194, 133–151.
- Goring, D.G., Nikora, V.I., 2002. Despiking acoustic Doppler velocimeter data. *J. Hydraul. Eng.* 128 (1), 117–126.
- Grare, L., Peirson, W.L., Branger, H., Walker, J.W., Giovanangeli, J.P., Makin, V., 2013. Growth and dissipation of wind-forced, deep-water waves. *J. Fluid Mech.* 722, 5–50.

- Hasselmann, K., 1971. On the mass and momentum transfer between short gravity waves and larger-scale motions. *J. Fluid Mech.* 50 (1), 189–205.
- Hussain, A., Reynolds, W., 1970. The mechanics of an organized wave in turbulent shear flow. *J. Fluid Mech.* 41 (2), 241–258.
- Kline, S., Reynolds, W., Schraub, F., Runstadler, P., 1967. The structure of turbulent boundary layers. *J. Fluid Mech.* 30 (4), 741–773.
- Li, D., Bou-Zeid, E., 2011. Coherent structures and the dissimilarity of turbulent transport of momentum and scalars in the unstable atmospheric surface layer. *Bound.-Lay. Meteorol.* 140 (2), 243–262.
- Longo, S., Chiapponi, L., Clavero, M., Mäkelä, T., Liang, D., 2012a. Study of the turbulence in the air-side and water-side boundary layers in experimental laboratory wind induced surface waves. *Coast. Eng.* 69, 67–81.
- Longo, S., Liang, D., Chiapponi, L., Jiménez, L.A., 2012b. Turbulent flow structure in experimental laboratory wind-generated gravity waves. *Coast. Eng.* 64, 1–15.
- Longo, S., Losada, M., 2012. Turbulent structure of air flow over wind-induced gravity waves. *Exp. Fluids* 53 (2), 369–390.
- Longuet-Higgins, M.S., 1987. The propagation of short surface waves on longer gravity waves. *J. Fluid Mech.* 177, 293–306.
- Longuet-Higgins, M.S., Stewart, R.W., 1960. Changes in the form of short gravity waves on long waves and tidal currents. *J. Fluid Mech.* 8 (4), 565–583.
- Mansard, E.P.D., Funke, E.R., 1980. The measurement of incident and reflected spectra using a least squares method. In: *Proc. 17th Coastal Engrg. Conf., Vol. 1. American Society of Civil Engineers*, pp. 154–172.
- Mori, N., Suzuki, T., Kakuno, S., 2007. Noise of acoustic Doppler velocimeter data in bubbly flows. *J. Eng. Mech.* 133 (1), 122–125.
- Olfateh, M., Ware, P., Callaghan, D.P., Nielsen, P., Baldock, T.E., 2017. Momentum transfer under laboratory wind waves. *Coast. Eng.* 121, 255–264.
- Peirson, W.L., Garcia, A.W., Pells, S.E., 2003. Water wave attenuation due to opposing wind. *J. Fluid Mech.* 487, 345–365.
- Sullivan, P.P., McWilliams, J.C., 2010. Dynamics of winds and currents coupled to surface waves. *Annu. Rev. Fluid Mech.* 42.
- Wallace, J.M., 2016. Quadrant analysis in turbulence research: history and evolution. *Annu. Rev. Fluid Mech.* 48, 131–158.
- Wallace, J., Brodkey, R., 1977. Reynolds stress and joint probability density distributions in the u-v plane of a turbulent channel flow. *Phys. Fluids* 20 (3), 351–355.